Self-duality of one-dimensional quasicrystals with spin-orbit interaction

Deepak Kumar Sahu,[1] Aruna Prasad Acharya,[1] Debajyoti Choudhuri,[2] and Sanjoy Datta[1,3,*]
[1]*Department of Physics and Astronomy, National Institute of Technology, Rourkela, Odisha-769008, India*
[2]*Department of Mathematics, National Institute of Technology, Rourkela, Odisha-769008, India*
[3]*Center for Nanomaterials, National Institute of Technology, Rourkela, Odisha-769008, India*

(Received 15 February 2021; accepted 14 July 2021; published 5 August 2021)

Noninteracting spinless electrons in one-dimensional quasicrystals, described by the Aubry-André-Harper (AAH) Hamiltonian with nearest-neighbor hopping, undergo a metal-to-insulator transition at a critical strength of the quasiperiodic potential. The AAH Hamiltonian is also known to be self-dual. Interestingly, the critical point and the self-dual point are identical in this case. In this work, we have studied the one-dimensional quasiperiodic AAH Hamiltonian in the presence of spin-orbit coupling of Rashba-type, which introduces an additional spin-conserving complex hopping and a spin-flip hopping. We have found that the AAH Hamiltonian remains self-dual in the presence of Rashba spin-orbit coupling, and the self-dual point follows a simple rescaled relationship among the parameters of the Hamiltonian. This system also undergoes a metal-to-insulator transition, and the nature of this transition has been found to be identical with the original AAH Hamiltonian. However, the critical points do not follow the same relationship as the self-dual points in general. In fact, the metal-to-insulator transition happens earlier than the self-dual point, except in some special cases in which they are observed to coincide.

DOI: 10.1103/PhysRevB.104.054202

I. INTRODUCTION

In a one-dimensional (1D) lattice with random disorder, all the electronic single-particle states of the noninteracting Anderson Hamiltonian localize exponentially even if the strength of the disorder is arbitrarily small [1,2]. In a pure Anderson Hamiltonian, the metal-to-insulator transition exists only in three dimensions, while in two dimensions there are no extended states, but for a weak disorder, single-particle states are marginally localized [2]. In contrast, a quasiperiodic lattice described by the Aubry-André-Harper Hamiltonian (AAH) [3–5] with nearest-neighbor hopping undergoes a metal-to-insulator transition (MIT) at a critical disorder strength, even in one dimension. Interestingly, the AAH Hamiltonian is also self-dual, unlike the Anderson Hamiltonian, and the self-dual point coincides exactly with the critical point. There had been an intense search for MIT in lower-dimensional systems with random disorder as well, which led to the understanding that the spin-orbit (SO) coupling can induce a MIT in such systems, at least in two dimensions [6–14]. By analogy to these results, it is expected that the SO coupling will have a similar antilocalization effect in quasiperiodic systems. However, it is also reasonable to expect that the SO coupling might have a nontrivial effect on the self-duality and the critical points since the localization mechanism in these two systems is not the same [15]. Moreover, it is not obvious whether the AAH Hamiltonian in the presence of SO coupling is self-dual or not, and if it is, then whether or not the metal-to-insulator transition takes place exactly at the self-dual point.

There have been studies on quasiperiodic 1D systems with SO coupling, mainly with broken time-reversal symmetry [16–19]. While Ref. [16] indicates the existence of self-duality in this system, the results of Refs. [18,19] suggest broken self-duality, although this has been attributed to the SO coupling and magnetic field, respectively. The broken time-reversal symmetric quasiperiodic systems are quite interesting in their own merit. However, as we are going to see, the question of self-duality, critical behavior, and their interrelationship in the time-reversal symmetric quasiperiodic systems with SO coupling requires closer attention as well.

To address these issues, in this work we have studied the AAH model with nearest-neighbor hopping in the presence of spin-orbit coupling of Rashba-type [20]. Our choice of this type of spin-orbit coupling is also motivated by the fact that it plays a crucial role in various device applications, especially in spintronic devices [21], which are built on the idea of controlling the electron's state by the external tuning of the Rashba spin-orbit (RSO) coupling, and this type of coupling is experimentally realizable in an optical setup as well. Localization in quasiperiodic systems has already been experimentally verified in the optical lattice experiments [22–25]. More recently, the critical behavior of the spinless version of the AAH Hamiltonian has also been experimentally observed in polaritonic 1D wires, created with the help of cavity-polariton devices [26]. In addition, SO coupling of Rashba-type has also been experimentally simulated in ultracold atomic systems [27–29]. Hence it is expected that, in the future, the Hamiltonian studied in this work can also be experimentally implemented in these setups, and our results are going to be a useful guide to these experiments.

*dattas@nitrkl.ac.in

The fundamental, spinless AAH Hamiltonian can be represented by the eigenvalue equation, $t(\psi_{n+1}+\psi_{n-1})+W\cos(2\pi bn+\phi)\psi_n = E\psi_n$, where W is the strength of the disorder, t is the nearest-neighbor hopping amplitude, and ψ_n is the amplitude of the electronic wave function at the lattice site n. When b is irrational, we obtain a quasiperiodic lattice. Irrespective of the filling factor, this original AAH Hamiltonian undergoes a metal-to-insulator transition at a critical strength of the quasiperiodic potential given by $W_c/t = 2$, where all the single-particle states are extended for $W/t < 2$ and localized for $W/t > 2$. At the critical point, all the states show multifractal character, that is, they are extended but *nonergodic*. Interestingly, the Fourier transformed AAH Hamiltonian, $\frac{W}{2}(\psi_{k+1}+\psi_{k-1})+2t\cos(2\pi bk+\phi)\psi_k = E\psi_k$, becomes the same as the real-space Hamiltonian when $W/t = 2$. Because of this unique feature, the AAH Hamiltonian is termed *self-dual*, and $W/t = 2$ is also known as the self-dual point.

In this work, we have found that in the presence of RSO coupling, the AAH Hamiltonian remains self-dual and undergoes a metal-to-insulator transition at a critical strength of the quasiperiodic potential, but the self-dual point and the critical point are not the same in general. While in the presence of RSO coupling the self-dual point follows a simple rescaled relationship between the parameters of the Hamiltonian, the critical points do not follow this relationship, although both values shift to a higher strength of the quasiperiodic potential with an increase in the RSO coupling strength. Interestingly, we have found that under special circumstances, the self-dual points are extremely close to our numerically estimated critical points. To determine the critical point precisely, we have used the idea of a many-body localization tensor, primarily developed to characterize the localization and the electric polarization simultaneously. The results of the localization tensor calculations indicate that the nature of the metal-to-insulator transition is identical to the original AAH Hamiltonian. For a better examination of the nature of this MIT, we have studied the behavior of the eigenstates in the metallic and insulating regimes, and at the critical point. To do this, first we have used the participation ratio and von Neumann entropy to get a quick overall idea, and then we carried out a detailed multifractal analysis to show that the eigenstates are indeed multifractal at the critical point, while all of them are extended below it and localized above it.

The paper is organized as follows: In Sec. II we introduce the Hamiltonian considered in this work. In Sec. III we present an analysis of the self-duality of our Hamiltonian, and we obtain an analytical expression of the self-dual point. The phase diagram has been discussed in Sec. IV, while in the subsequent subsections we present our method and results to determine the phase diagram. Then we proceed to present our participation ratio and the von Neumann entropy analysis in Secs. V and VI, respectively. Finally, in Sec. VII we present the multifractal analysis of the eigenstates.

II. AUBRY-ANDRÉ MODEL WITH RSO COUPLING

The Hamiltonian considered in this work consists of two parts,

$$H' = H + H_R, \tag{1}$$

where H is the usual AAH Hamiltonian given by

$$H = -t\sum_{i=1,\sigma}^{L-1}(c^\dagger_{i+1,\sigma}c_{i,\sigma} + \text{H.c.}) + W\sum_{i=1,\sigma}^{L}\cos(2\pi bi+\phi)c^\dagger_{i,\sigma}c_{i.\sigma}. \tag{2}$$

Here, t is the hopping amplitude from site i to site $i+1$, and $L = Na$ is the length of the lattice, where N is the number of lattice sites and $a = 1$ (arbitrary unit) is the lattice spacing. $c^\dagger_{i,\sigma}$ and $c_{i,\sigma}$ are the fermionic creation and annihilation operators, respectively, for the particle at the site i having spin σ ($\sigma = \uparrow, \downarrow$). W is the strength of the quasiperiodic potential. ϕ is an arbitrary phase varying from $(0, 2\pi)$. The choice of the phase ϕ does not affect our conclusion, and henceforth we shall set it to zero. We have used $b = (\sqrt{5}+1)/2$. It is important to note that sometimes in the literature $b = (\sqrt{5}-1)/2$ is also used, but our conclusions are independent of the particular choice of b.

The RSO Hamiltonian H_R is given by [30]

$$H_R = -\alpha_z\sum_{i=1,\sigma,\sigma'}^{L-1}[c^\dagger_{i+1,\sigma}(i\sigma_y)_{\sigma,\sigma'}c_{i,\sigma'} + \text{H.c.}] - \alpha_y\sum_{i=1,\sigma,\sigma'}^{L-1}[c^\dagger_{i+1,\sigma}(i\sigma_z)_{\sigma,\sigma'}c_{i,\sigma'} + \text{H.c.}], \tag{3}$$

where σ_y and σ_z are Pauli spin matrices in the y- and z-directions, respectively. α_y is a complex spin-conserving hopping due to the confinement in the y-direction, and α_z is a spin-flip hopping due to the confinement in the z-direction. The hopping amplitude α_y and α_z could be different in general, and they could also be site-dependent. The pure RSO Hamiltonian H_R, which is studied in this work, has also been studied in the context of transport properties in quantum nanowires [31,32]. Also, localization properties of attractive fermions have been studied recently in the presence of the spin-flip component of the RSO Hamiltonian [33].

III. SELF-DUALITY OF THE AAH HAMILTONIAN IN THE PRESENCE OF RSO

To understand the self-duality of the AAH Hamiltonian in the presence of RSO, we start with the stationary Schrödinger equation $H|\Psi\rangle = E|\Psi\rangle$, where $|\Psi\rangle = \sum_{n,\sigma}\psi^\sigma_n c^\dagger_{n,\sigma}|0\rangle$. In real space, we obtain the following set of coupled eigenvalue equations:

$$-t(\psi^\uparrow_{n+1}+\psi^\uparrow_{n-1}) + \alpha_y(e^{-i\pi/2}\psi^\uparrow_{n+1} + e^{i\pi/2}\psi^\uparrow_{n-1}) + \alpha_z(\psi^\downarrow_{n+1}-\psi^\downarrow_{n-1}) + W\cos(2\pi bn+\phi)\psi^\uparrow_n = E\psi^\uparrow_n, \tag{4}$$

$$-t(\psi^\downarrow_{n+1}+\psi^\downarrow_{n-1}) + \alpha_y(e^{-i\pi/2}\psi^\downarrow_{n+1} + e^{i\pi/2}\psi^\downarrow_{n-1}) - \alpha_z(\psi^\uparrow_{n+1}-\psi^\uparrow_{n-1}) + W\cos(2\pi bn+\phi)\psi^\downarrow_n = E\psi^\downarrow_n. \tag{5}$$

Multiplying Eq. (5) by i and adding it to Eq. (4), the two coupled eigenvalue equations can be combined into a single equation as follows:

$$\gamma[e^{-i\eta}\tilde{\psi}_{n+1} + \tilde{\psi}_{n-1}e^{i\eta}] + W\cos(2\pi bn+\phi)\tilde{\psi}_n = E\tilde{\psi}_n, \tag{6}$$

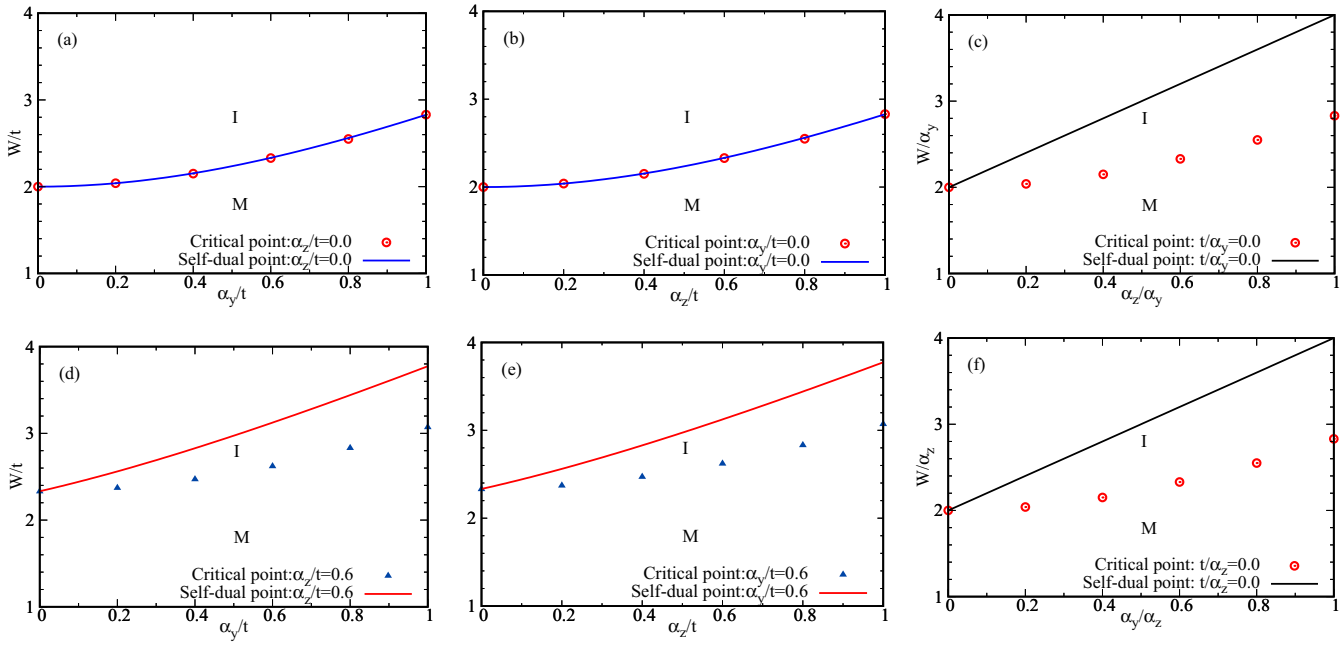

FIG. 1. The metal (M) to insulator (I) transition and self-duality of the AAH Hamiltonian in the presence of RSO coupling. The phase diagrams have been plotted in the parameter space spanned by the strength of quasiperiodic potential W and the RSO coupling. The critical points are plotted for a half-filled system. However, they are independent of filling fraction (see Sec. V). (a), (b) Comparison of the self-dual line with the critical points when α_y, the spin-conserving complex hopping amplitude of the RSO Hamiltonian, is nonzero, while α_z, the spin-flip hopping component, is zero, and vice versa. In both of these cases, the self-dual lines match extremely well with our estimated critical points. Numerical data are presented in Table I. (d), (e) Comparison of the self-dual line with the critical points as a function of α_y ($\alpha_z/t = 0.6$) and α_z ($\alpha_y/t = 0.6$). The self-dual line and the critical points are separated except when $\alpha_y/t = 0$ or $\alpha_z/t = 0$. (c), (f) In both of these cases, t has been set to zero and the critical points have been computed as a function of α_z and α_y. It is clear that the critical points are identical to (a) or (b), but they do not coincide with the self-dual line.

where $\tilde{\psi}_n = \psi_n^{\uparrow} + i\psi_n^{\downarrow}$, $\gamma = \sqrt{t^2 + (\alpha_y + \alpha_z)^2}$, and $\eta = \tan^{-1}[-(\alpha_y + \alpha_z)/t]$. The above eigenvalue equation is equivalent to the original AAH Hamiltonian, except for the extra phase factor in the effective hopping amplitude γ. However, a constant phase factor in the hopping amplitude does not affect the self-duality. To see this explicitly, we first apply the transformation $\tilde{\psi}_n = \sum_k \tilde{\psi}_k e^{i(2\pi bn+\phi)k}$ in Eq. (6) to obtain the momentum space equation as follows:

$$2\gamma\cos(2\pi bk - \eta)\tilde{\psi}_k + \frac{W}{2}(\tilde{\psi}_{k+1} + \tilde{\psi}_{k-1}) = E\tilde{\psi}_k, \qquad (7)$$

where $\tilde{\psi}_k = \psi_k^{\uparrow} + i\psi_k^{\downarrow}$. Now, applying the inverse Fourier transformation $\tilde{\psi}_k = \sum_n \tilde{\psi}_n e^{-i(2\pi bk-\eta)n}$ in Eq. (7), we finally obtain the following eigenvalue equation in real space:

$$\gamma[\tilde{\psi}_{n+1} + \tilde{\psi}_{n-1}] + W\cos(2\pi bn)\tilde{\psi}_n = E\tilde{\psi}_n. \qquad (8)$$

The above expression is exactly identical with the original AAH eigenvalue equation ($\phi = 0$), with a rescaled hopping amplitude γ. Hence, the AAH Hamiltonian is also self-dual like the original AAH Hamiltonian in the presence of RSO coupling, with the self-dual point being $W_s/t = 2\sqrt{1 + (\alpha_y/t + \alpha_z/t)^2}$. It is important to note that Eq. (6) could also have been obtained by choosing $\tilde{\psi}'_n = \psi_n^{\downarrow} - i\psi_n^{\uparrow}$.

IV. ANALYSIS OF THE PHASE DIAGRAM

From the analytical expression of the self-dual point, it is obvious that when each of the three hopping processes is considered separately with the quasiperiodic potential, we recover a self-duality condition for each of them, given by $W_s/t = 2$, $W_s/\alpha_y = 2$, and $W_s/\alpha_z = 2$, respectively. For the original AAH Hamiltonian, the self-dual point and the critical point are identical. In analogy with this, we also expect the metal-to-insulator transition to take place at the self-dual point when only α_y or α_z is considered with the quasiperiodic potential. We have verified this numerically, and the results are presented in Appendix A. We have also found that the critical point and the self-dual point coincide with each other in the two limiting cases (i) $\alpha_y = 0$ and (ii) $\alpha_z = 0$. In Figs. 1(a) and 1(b), we have plotted the self-dual line along with the critical points, obtained after solving the eigenvalue equations numerically, for these two special cases. It is evident that, within the accuracy of our numerical calculations, the critical points and the self-dual line agree with each other extremely well in both cases. Furthermore, the critical points are the same in Figs. 1(a) and 1(b). However, the critical point, W_c/t, does not coincide with the self-dual point when all three hopping processes have nonzero amplitude. Surprisingly, when both α_y and α_z are nonzero, then the critical points and the self-dual line get separated from each other, with the separation getting larger with the increase in the RSO coupling strength. These results are plotted in Figs. 1(d) and 1(e). It is clear that in these cases, $W_c/t < W_s/t$ always. However, there are some striking similarities between the behavior of the self-dual points and the critical points in general. Like the self-dual points, the critical points are identical for $\alpha_y/t = c_1, \alpha_z/t = c_2$

and $\alpha_y/t = c_2, \alpha_z/t = c_1$, where c_1 and c_2 are some constants.

To understand the origin of this mismatch between the critical point and the self-dual point, in Figs. 1(c) and 1(f) we have considered the special case when the tight-binding hopping amplitude, t, is zero. In Fig. 1(c) we have studied the critical behavior of the resulting Hamiltonian as a function of the spin-flip hopping amplitude α_z, measured in units of α_y, while α_y, measured in units of α_z, has been chosen as the independent parameter in Fig. 1(e). From the analytical expression of the self-dual point, it is easy to see that, in this special case, the self-dual points follow the equation of a straight line. However, the critical points remain identical to the cases when $\alpha_y = 0$ or $\alpha_z = 0$. Naturally, the critical points and the self-dual line do not coincide with each other. Hence, the separation between the critical and the self-dual points in the full Hamiltonian can be attributed to the combined effect of the two hopping processes of the RSO Hamiltonian.

A. Kohn's localization tensor and the metal-to-insulator transition

It is tempting to conclude, in analogy with the original AAH Hamiltonian, that the metal-to-insulator transition takes place exactly at the location of the self-dual point in the presence of RSO coupling as well. However, from the discussion of the phase diagram we have found that one has to be very careful before drawing any such conclusion from the analytical expression of the self-dual point directly. In fact, to compare the two aspects, it is imperative to determine the critical points with a high degree of accuracy. In this section, we present our method to determine the critical point precisely and discuss the key results for a half-filled system. To locate the critical points, we have used the idea of Kohn's localization tensor. It is a reliable way to characterize metallic and insulating states.

Based on the idea first proposed by Kohn [34], Resta and Sorella [35,36] formulated a localization tensor $\lambda_{\alpha\beta}$, alternatively known as Kohn's localization tensor, to describe polarization and localization in terms of a single many-body expectation value z_N^{α}. Here, α and β are the spatial coordinates. It is independent of system sizes for insulating states, while for metallic states it diverges as system size becomes infinite. It is important to note that $\lambda_{\alpha\beta}$ is a measure of the many-body localization length, and it does not indicate the spatial extent of single-particle eigenstates. In the case of a noninteracting band insulator, it is related to the spatial extent of maximally localized Wannier functions [37]. However, for disordered systems, a similar conclusion cannot be drawn. Nevertheless, recently it has been shown [38] that the localization tensor can capture the metal-to-insulator transition accurately in the 1D AAH model. In this work, we have found that it can also be used to locate the critical point quite accurately in the presence of RSO coupling.

Here, we briefly discuss the key aspects of the localization tensor and methods to calculate it for different boundary conditions [38–40]. A more elaborate discussion on the localization tensor and ways to compute it can be found in Ref. [39] and in Ref. [41]. For the periodic boundary condition (PBC), the localization tensor, $\lambda_{\alpha\beta}$ (here $\alpha = x, \beta = x$), can be expressed as

$$\lambda_{xx}^2 = -\frac{L^2}{4\pi^2 N} \ln \frac{\left|z_N^x\right|\left|z_N^x\right|}{\left|z_N^{xx}\right|}, \tag{9}$$

where the quantity z_N^x is given by

$$z_N^x = \langle \Psi | e^{i\frac{2\pi}{L}\hat{\mathbf{R}}_x} | \Psi \rangle, \tag{10}$$

whereas $z_N^{\alpha\beta}$ can be obtained by replacing $\hat{R}_\alpha$ with $\hat{R}_\alpha - \hat{R}_\beta$. Hence, in our case, $|z_N^{xx}| = 1$. In the above equation, $|\Psi\rangle$ is the many-body ground-state wave function, and $\hat{\mathbf{R}} = \sum_{i=1}^{N} \hat{r}_i$ is the many-body position operator, with $\hat{\mathbf{R}}_x$ being the x component. For a half-filled system ($L = N$) in one dimension, the localization tensor reduces to

$$\lambda_{xx}^2 = \lambda^2 = -\frac{L}{2\pi^2} \ln\{|z_N|\}. \tag{11}$$

In the absence of electron-electron interaction, $z_N^{(x)}$ can be simplified further [39,40] and represented as $z_N^{(x)} = \det^2[S_{jj'}^x]$, where $S_{jj'}^x$ is a matrix whose elements are given by

$$S_{j,j'}^x = \int dr\, \psi_j^*(r) e^{i\frac{2\pi}{L}\hat{r}_x} \psi_{j'}(r). \tag{12}$$

In the above equation, $\psi_j(r)$ represents the amplitude of a single-particle wave function at position r for a spin-up or spin-down electron arranged in order of increasing energies. The indices j and j' indicate the energy level. Since, in the absence of RSO coupling, spin-up and spin-down electrons are completely decoupled, it is sufficient to consider only one type of spin and $j, j' = 1, 2, \ldots, N/2$ to compute λ_{xx}^2 at half-filling. However, in the presence of RSO, and more specifically because of the spin-flip hopping process, in Eq. (12) $\psi_j(r)$ now represents the amplitude of a single quasiparticle wave function at position r corresponding to the jth eigenenergy. Hence, in our case, $j, j' = 1, 2, \ldots, N$.

In the case of open boundary conditions (OBCs), the squared localization length (λ^2), in units of the nearest-neighbor distance, can be expressed as follows [41,42]:

$$\lambda^2 = \frac{1}{\nu N} \sum_{i,i'=1}^{N} |\rho_{ii'}(\nu)|^2 (i - i')^2, \tag{13}$$

where $i, i' = 1, \ldots, N$ represents the lattice site, ν is the filling factor, and $\rho_{ii'}(\nu)$ is the one-body density matrix defined as

$$\rho_{ii'} = \sum_{j=1}^{N} \psi_j(i) \psi_j^*(i'), \tag{14}$$

where $\psi_j(i)$ is the amplitude of a single quasiparticle wave function at lattice site i, corresponding to the jth eigenvalue. Since we are interested to compute λ^2 at half-filling, we set $\nu = 1$ in Eq. (13). However, our conclusions are independent of filling fractions. In Appendix B, we have presented results for a quarter-filled system, which are identical to those of a half-filled system. It is important to note that there could be some special filling fraction when the system does not show any metal-to-insulator transition. We have discussed this issue in Sec. V.

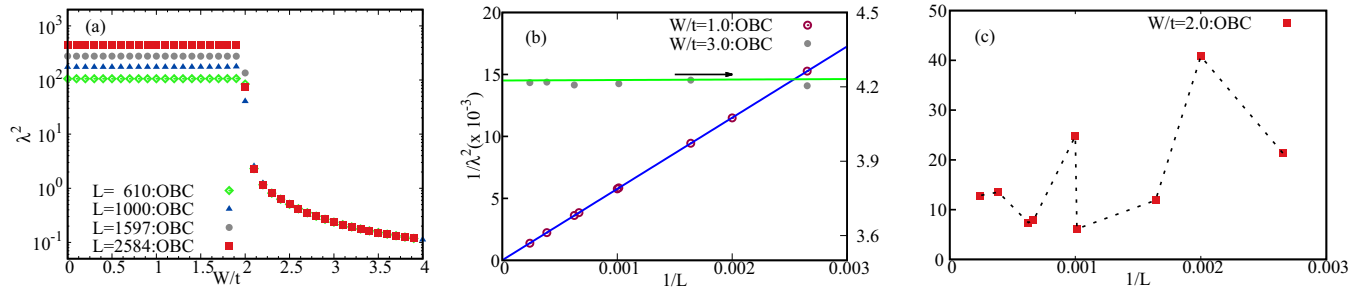

FIG. 2. (a) Squared localization length λ^2 for the half-filled 1D pure AAH model with respect to disorder strength W/t for some selected lattices. (b) Scaling of inverse localization length $1/\lambda^2$ with inverse chain length $(1/L)$. For finite-size scaling, we have used $1/\lambda^2 = a_0 + b_0/L$. (c) Plot of $1/\lambda^2$ with $1/L$ at the critical point. It is evident that at the critical point, $1/\lambda^2$ does not follow the scaling pattern of either metallic or insulating states. All the results are for the open boundary condition.

1. Localization tensor without RSO

Before presenting the localization tensor results for our Hamiltonian, in this section, we first benchmark our λ^2 calculations for the original AAH Hamiltonian at half-filling. We also highlight the behavior of λ^2 with varying system sizes at the critical point. In Figs. 2 and 3, we have shown these results for open and periodic boundary conditions respectively. In case of PBC, the system sizes are restricted to lattice sizes, given by the Fibonacci sequence, while for OBC there is no such restriction. We have found that the critical behavior is independent of the boundary conditions.

In Figs. 2(a) (OBC) and 3(a) (PBC), we have shown the variation of squared localization length λ^2 with increasing disorder strength (W/t) for different 1D lattices at the half-filling. As expected, the transition from delocalized to localized phase occurs at $W_c/t \simeq 2$ for both the boundary conditions. The λ^2 values are finite and independent of system sizes above $W/t > 2$, whereas for $W/t < 2$, it increases with the increase in system size. These observations are similar to Ref. [38]. From the plots of $1/\lambda^2$ versus $1/L$ in Figs. 2(b) and 3(b), it is clear that, irrespective of the boundary condition, λ^2 diverges for $L \to \infty$ in the metallic phase, while it is nearly constant and converges to a finite value in the insulating phase. For pure AAH Hamiltonian, we have found that $1/\lambda^2$ scales linearly with the inverse of the system size. For finite-size scaling, we have used $1/\lambda^2 = a_0 + b_0/L$, where a_0 and b_0 are two adjustable parameters.

At the critical point $W_c/t = 2$, scaling behavior of λ^2 with an increase in the system size is expected to be erratic as all the single particle eigenstates are multifractal in case of pure AAH model. However, it can be an useful indicator to detect the existence of multifractal eigenstates within a spectrum. Since there is no characteristic length-scale for the multifractal states, we can expect an anomalous behaviour of $1/\lambda^2$ with respect to $1/L$ compared to the pure metallic and insulating phases. In Figs. 2(c) and 3(c) we have plotted $1/\lambda^2$ versus $1/L$ for $W_c/t = 2$. In the case of OBC, it is clear that λ^2 neither converges to a finite value, nor does it approach to zero in the limit when L becomes very large. With PBC, λ^2 oscillates with increasing L without any indication of convergence.

2. Localization tensor in the presence of RSO

We now present our localization tensor results for the one-dimensional AAH model in the presence of RSO coupling. To illustrate the effect of RSO on the critical point, in this section we primarily focus on the $\alpha_y = 0$ case. In the next section, we have presented the results for the other cases. Here, we have used $\alpha_z/t = 0.8$. There is nothing special about this value, as all our conclusions are independent of it, except the location of the critical point. In Figs. 4(a) (OBC) and 5(a) (PBC), the variation of the squared localization length λ^2 with an increasing value of the disorder strength W/t have been shown. It is obvious that in the presence of the RSO coupling, the localization tensor is qualitatively identical to the original AAH Hamiltonian. However, the critical point has shifted to higher disorder strength given by $W_c/t \simeq 2.5$.

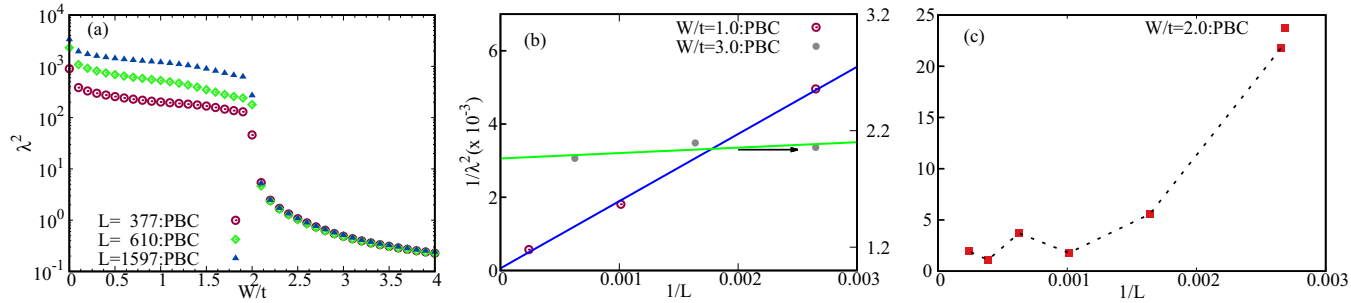

FIG. 3. Localization tensor λ^2 for the half-filled 1D pure AAH model with PBC. (a) λ^2 vs W/t for a few selected chain lengths. (b) Finite-size scaling of $1/\lambda^2$ vs $(1/L)$. (c) Once again, similar to the OBC case, $1/\lambda^2$ lacks simple scaling behavior with $1/L$ at the critical point.

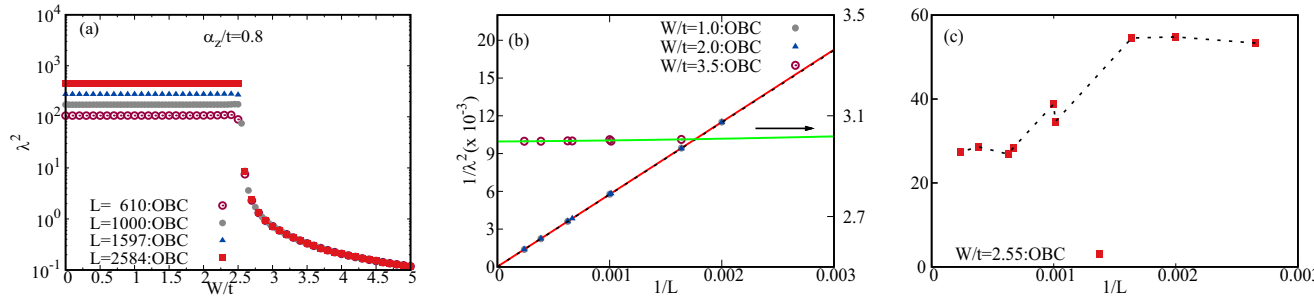

FIG. 4. The localization tensor λ^2 for a half-filled 1D AAH model with RSO coupling. (a) λ^2 vs W/t for selected lattices with OBC. (b) Scaling of inverse localization length $1/\lambda^2$ vs $1/L$. Here, $1/\lambda^2$ scales linearly with $1/L$ similar to Fig. 2(b). (c) Plot of $1/\lambda^2$ vs $1/L$ at the critical point $W_c/t = 2.55$. Lack of proper scaling of $1/\lambda^2$ indicates that our estimation of the critical point is quite correct.

The above observations have been further validated with the finite-size scaling of $1/\lambda^2$ below and above the critical point. These results are presented in Figs. 4(b) and 5(b). In the case of OBC, it is clear that $1/\lambda^2$ converges to zero as $L \to \infty$ for $W/t < 2.5$, as expected for a delocalized phase. On the other hand, as expected in the case of an insulating phase, the localization tensor is independent of system size for $W/t > 2.5$. In the case of PBC, these fundamental conclusions remain the same. Interestingly, however, with PBC, the dependence of $1/\lambda^2$ on $1/L$ deviates significantly in the presence of RSO in the metallic phase. For finite-size scaling, especially for the metallic phase, we have used $1/\lambda^2 = a_0 + b_0/L + c_0/L^2$, where a_0, b_0, and c_0 are adjustable parameters.

It is easy to pinpoint the critical disorder strength from the λ^2 versus W/t data almost exactly. We are going to see that this information can also be reliably extracted from the multifractal analysis (Sec. VII A). From the localization tensor result, we estimate $W_c/t = 2.55$ for $\alpha_z/t = 0.8$ with a maximum error of $\delta W_c/t = \pm 0.01$. In Appendix C, we have shown the variation of λ^2 around the critical point to illustrate the accuracy of this estimation. A similar analysis has been performed to determine the phase boundaries. To cross-check this estimation, we have also plotted $1/\lambda^2$ versus $1/L$ separately at $W_c/t = 2.55$ in Figs. 4(c) and 5(c). It is quite clear that $1/\lambda^2$ does not follow any discernible pattern with $1/L$.

B. Evolution of the critical point with RSO interaction

In this section, we first study the evolution of the critical point for two limiting cases, i.e., (i) $\alpha_y = 0$ and (ii) $\alpha_z = 0$. We then present the results for the general case where $\alpha_z \neq 0$ and $\alpha_y =$ fixed, and vice versa. We have found in the previous sections that the critical behavior is independent of the boundary conditions. Hence, in this section, the results are presented only for OBC and for a lattice having $N = 1597$ sites. In Fig. 6(a), we have considered only the spin-flip hopping α_z in the RSO Hamiltonian. It is clear, even from the results for a single finite lattice, that the critical point moves to a higher strength of the quasiperiodic potential with an increase in the RSO coupling strength. In Fig. 6(b), we present the results for the limiting scenario when $\alpha_y \neq 0$ and $\alpha_z = 0$. It is clearly evident that the effect on the critical point is exactly identical to the previous case. Exactly similar trends have been found when the tight-binding hopping amplitude t is set to zero. These results have been presented in Appendix D.

Figure 6(c) represents the general nature of the evolution of the critical point when the full RSO Hamiltonian is considered along with the original AAH Hamiltonian. As expected, in the presence of both the spin-preserving and spin-flip components of the RSO Hamiltonian, the critical point is pushed further to a higher disorder strength. It is interesting to observe that the critical point is the same for the two possible combinations for which the condition $(\alpha_y + \alpha_z)/t = c$, where c is a constant, is satisfied. This relationship between the critical point and the SO coupling terms is similar to that of the self-dual point, although the metal-to-insulator transition happens earlier. In Table I, we have presented the critical points estimated from the localization tensor calculations and compared with the self-dual point obtained from the analytical expression. It is clear that the critical point and the self-dual point agree

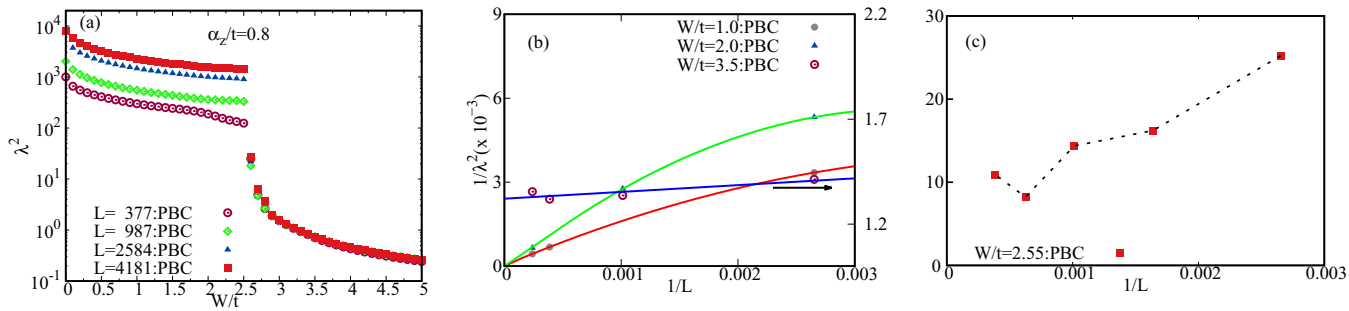

FIG. 5. The localization tensor λ^2 for a half-filled 1D AAH model with RSO coupling. (a) λ^2 vs W/t for selected lattices with PBC. (b) Finite-size scaling of $1/\lambda^2$ with inverse chain length $1/L$, below and above the critical point. We have used $1/\lambda^2 = a_0 + b_0/L + c_0/L^2$ for scaling in the metallic phase. (c) With PBC as well, we find anomalous behavior of $1/\lambda^2$ with increasing system size at $W/t = 2.55$.

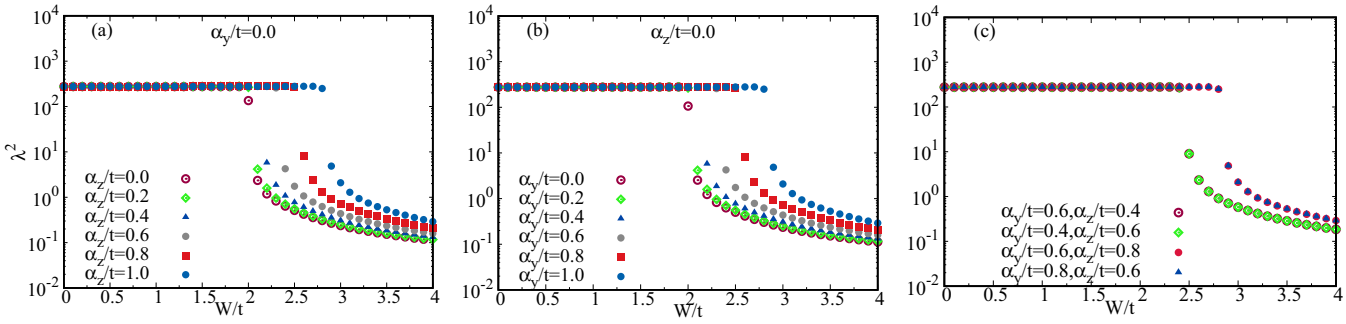

FIG. 6. (a) Evolution of the self-dual point in the AAH with only spin-flip hopping induced by RSO coupling. The results are for a lattice $L = 1597$ with OBC. (b) The self-dual point moves toward higher strength of the quasiperiodic potential when the pure AAH Hamiltonian is considered with only the complex hopping induced by the RSO coupling. (c) Evolution of the self-dual point when the AAH Hamiltonian is considered with the full RSO Hamiltonian. Here we have shown the change in the critical point for $\alpha_y/t + \alpha_z/t = 1.0$ and 1.4. For each case there are two possibilities, and the critical point is the same for these different possibilities. This behavior is identical in nature with the self-dual point, although the self-dual points are different.

extremely well when $\alpha_y = 0$ or $\alpha_z = 0$, while they differ from each other for the general case.

V. PARTICIPATION RATIO

The existence of the MIT in the presence of RSO is evident from the results of the localization tensor calculations. Although at the critical point an anomalous behavior of the localization tensor with the inverse of the system size does indicate the absence of a characteristic length scale, the true nature of the quasiparticle eigenstates across the entire energy spectrum is not clear. For example, if an energy spectrum contains predominantly delocalized states, then the localization tensor can suppress the contribution of the localized states while calculating it up to a certain filling fraction. To distinguish the localized and delocalized states, the participation ratio (PR) is regularly used as a first indicator. PR can also provide some hint, although only qualitatively, of multifractal eigenstates, if it exists. Generally, PR is used to immediately identify the existence of a mobility edge. Typically, a mobility edge is defined as the energy that separates localized and delocalized eigenstates in the energy spectrum. If a mobility edge exists, the PR jumps from a system-size-independent (insulating/localized states) higher value to a lower value (ergodic metallic/extended states) that scales inversely with the system size. In our case, we have observed that away from the critical point, the states are either delocalized ($W < W_c$) or localized ($W > W_c$). The other important question that remains to be answered is, what is the nature of the eigenstates at the critical point?

TABLE I. Numerically determined critical points from the localization tensor. All the quantities are represented relative to the tight-binding hopping amplitude t. The critical points (not shown here for brevity) are the same as the second column when $t = 0$, and W_c is measured with respect to either α_y or α_z. Numerical values of W_s (presented only up to the third decimal place) have been calculated from the analytical expression.

$\alpha_{z/y}$	W_c (± 0.01) ($\alpha_{y/z} = 0$)	W_s ($\alpha_{y/z} = 0$)	W_c (± 0.01) ($\alpha_{y/z} = 0.6$)	W_s ($\alpha_{y/z} = 0.6$)
0.0	2.00	2.000	2.33	2.332
0.2	2.04	2.039	2.37	2.561
0.4	2.15	2.154	2.47	2.828
0.6	2.33	2.332	2.62	3.124
0.8	2.55	2.561	2.83	3.441
1.0	2.83	2.828	3.07	3.773

In the AAH model without RSO, all the eigenstates are extended but nonergodic at the critical point. PR data qualitatively indicate that RSO does not alter this behavior. At this point, we would like to mention that, studying the single-particle energy spectra E_n and the distribution of the level-spacing $\delta_n = E_{n+1} - E_n$ can also reveal a great deal about the nature of the eigenstates [43–45]. Typically, the energy spectrum of the AAH Hamiltonian consists of subbands and many gaps between these subbands. Recently, it has been reported that there are some special states inside these subband gaps [46] which are localized even in the metallic phase of the pure AAH Hamiltonian. We have checked that these states are mostly concentrated at the lattice edges. These states may or may not appear, depending on the combination of various factors, such as the boundary conditions, the system size, and the irrational number b. As long as the filling is not fixed up to these special states, these states do not influence the critical behavior in any way. However, if the system is filled up to these special states, then there is no metal-to-insulator transition. In fact, the system behaves like an insulator, as expected. In Appendix E, we have presented some results to demonstrate this.

Formally, for the νth quasiparticle eigenstate, the usual definition of PR [47] can be generalized as follows:

$$P_\nu(q) = \sum_\sigma \sum_{i=1}^{N} |\psi_{\nu,\sigma}(i)|^{2q}, \quad q = 2. \tag{15}$$

Here the νth single quasiparticle eigenstate is given by $|\Psi_\nu\rangle = \sum_\sigma \sum_{i=1}^{N} \psi_{\nu,\sigma}(i)\,|1,\sigma\rangle_i$, where $|1,\sigma\rangle_i = |0,0,\ldots,\sigma_i,\ldots,0,0\rangle$ represents the localized basis state having one particle with spin σ at site i. Since this is a noninteracting problem, the usual scaling properties with respect to system size are also expected to hold for the

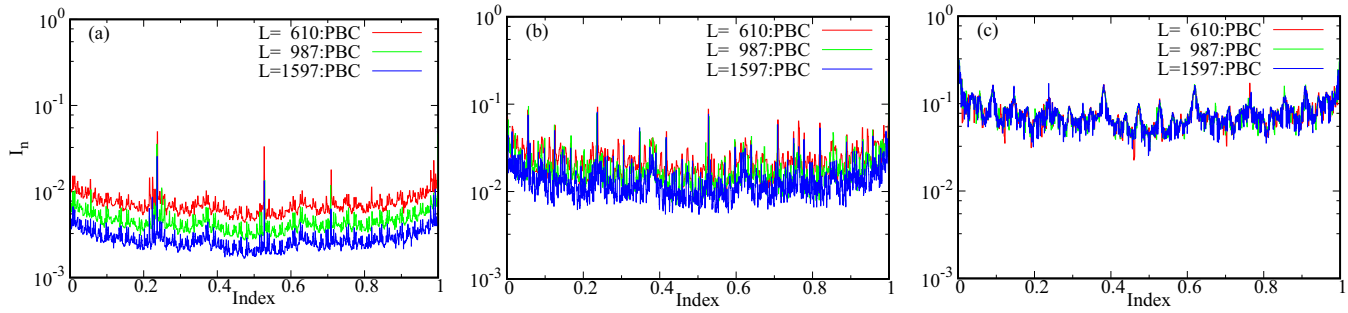

FIG. 7. Evolution of PR I_n with increasing disorder strength for a fixed RSO coupling $\alpha_z/t = 0.8$ and $\alpha_y = 0$. (a) $W/t = 2.5$, (b) $W/t = 2.55$, and (c) $W/t = 2.6$. Here the index represents the ratio of serial number of eigenstates to total number of eigenstates $[i/(2L)]$, where $i = 1, 2, \ldots, 2L$.

quasiparticle states, i.e., for a perfectly extended metallic state $P_\nu(q) = 1/N$, and for a completely localized state $P_\nu(q) = 1$. For a localized state, the PR value is supposed to be system-size-independent. These distinct scaling properties of PR enable it to identify delocalized and localized states quickly. We have numerically verified that the spin-up and spin-down contributions are identical to the PR of the quasiparticle they constitute.

In Fig. 7, we have plotted the PR spectrum for (a) $W/t = 2.5$, (b) $W/t = 2.55$, and (c) $W/t = 2.6$. These results are for $\alpha_z/t = 0.8$, $\alpha_y/t = 0$. It is evident that for $W/t < 2.55$, all the eigenstates are delocalized as the PR value in this region depends inversely on the system size across the entire energy spectrum, while all the states are localized for $W/t > 2.55$. On the other hand, at the critical point the PR spectrum behaves differently, i.e., it is neither independent of system size nor does it scale inversely with L like the extended states. This behavior is similar to the PR spectrum of the AAH model without RSO at the critical point, i.e., these are multifractal. Furthermore, the correlation between the energy level-spacing spectra and the scaling behavior of PR with L for all three different types of electronic states is similar to the AAH model without RSO [46]. In the delocalized phase, PR typically behaves inversely with L across the whole energy spectrum, except at the special positions, where the level spacing jumps abruptly. At the critical point, both of them show anomalous behavior with the system size, while in the localized phase the PR spectrum behaves opposite as compared to the delocalized phase at these special points of level-spacing spectra apart from being system-size-independent. All of these results are presented for PBC. OBC does not change any fundamental conclusions.

VI. von NEUMANN ENTROPY

From the results of the previous sections, it is evident that at the half-filling there is a transition from the metallic phase to an insulating phase at a critical disorder strength $W_c/t > 2.0$, which increases as the strength of RSO is increased. Furthermore, these results also hint that at the critical point the states are multifractal, a preliminary observation that we are going to establish firmly in Sec. VII. In this section, we present the results of the von Neumann entropy (vNE), an alternative indicator of single-particle properties, which can also be used to qualitatively identify the nature of the eigenstates.

In the case of noninteracting spin-1/2 fermions, and in the presence of RSO coupling, the individual eigenstates are occupied by quasiparticles. The quasiparticle eigenstate having energy E_ν can be written as

$$|\Psi_\nu\rangle = \sum_{i=1}^{N} \left[\psi^\nu_{i,\uparrow}|1,\uparrow\rangle_i + \psi^\nu_{i,\downarrow}|1,\downarrow\rangle_i\right], \tag{16}$$

where $|1,\uparrow\rangle_i = |1\rangle_i \otimes |\uparrow\rangle$ and $|1,\downarrow\rangle_i = |1\rangle_i \otimes |\downarrow\rangle$. $|1,\uparrow\rangle_i = c^\dagger_{i,\uparrow}|0\rangle$ and $|1,\downarrow\rangle_i = c^\dagger_{i,\downarrow}|0\rangle$. Here $|0\rangle$ represents the vacuum state for the lattice in a real-space basis. $c^\dagger_{i,\uparrow}$, $c^\dagger_{i,\downarrow}$ are the creation operators for spin-up and spin-down particles, respectively, at the lattice site i. The average number of spin-up and spin-down particles at site i is given by $|\psi^\nu_{i,\uparrow}|^2 = \langle\Psi_\nu|c^\dagger_{i,\uparrow}c_{i,\uparrow}|\Psi_\nu\rangle$ and $|\psi^\nu_{i,\downarrow}|^2 = \langle\Psi_\nu|c^\dagger_{i,\downarrow}c_{i,\downarrow}|\Psi_\nu\rangle$, respectively. Then, the local density matrix ρ^ν_j can be obtained from the total density matrix ρ^ν by tracing over all the lattice sites except site j, and it can be written as

$$\begin{aligned}\rho^\nu_j = {} & \left|\psi^\nu_{j,\uparrow}\right|^2|1,\uparrow\rangle_j\langle 1,\uparrow|_j + \left(1-\left|\psi^\nu_{j,\uparrow}\right|^2\right)|0,\uparrow\rangle_j\langle 0,\uparrow|_j \\ & + \left|\psi^\nu_{j,\downarrow}\right|^2|1,\downarrow\rangle_j\langle 1,\downarrow|_j + \left(1-\left|\psi^\nu_{j,\downarrow}\right|^2\right)|0,\downarrow\rangle_j\langle 0,\downarrow|_j.\end{aligned} \tag{17}$$

It is important to note that $|0,\uparrow\rangle_j$ and $|0,\uparrow\rangle_j$ represent the local vacuum states for jth site. A similar interpretation applies to the states $|1,\uparrow\rangle_j$ and $|1,\downarrow\rangle_j$. The von Neumann entropy for spin-1/2 quasiparticles follows easily from Eq. (17) as

$$\begin{aligned}S^{\rm nis}_{j,\nu} = {} & -\left(\left|\psi^\nu_{j,\uparrow}\right|^2\log_2\left|\psi^\nu_{j,\uparrow}\right|^2 + \left(1-\left|\psi^\nu_{j,\uparrow}\right|^2\right)\ln\left(1-\left|\psi^\nu_{j,\uparrow}\right|^2\right)\right) \\ & - \left(\left|\psi^\nu_{j,\downarrow}\right|^2\ln\left|\psi^\nu_{j,\downarrow}\right|^2 + \left(1-\left|\psi^\nu_{j,\downarrow}\right|^2\right)\ln\left(1-\left|\psi^\nu_{j,\downarrow}\right|^2\right)\right).\end{aligned} \tag{18}$$

Finally, summing over all the lattice sites, the von Neumann entropy for a quasiparticle eigenstate is defined as

$$S^{\rm nis}_\nu = \sum_{j=1}^{N} S^{\rm nis}_{j,\nu}. \tag{19}$$

Similar to the spinless AA model, for a purely extended quasiparticle state $S^{\rm nis}_\nu \approx (\log_2 N + 1)$, and for a completely localized state $S^{\rm nis}_\nu \approx 0$.

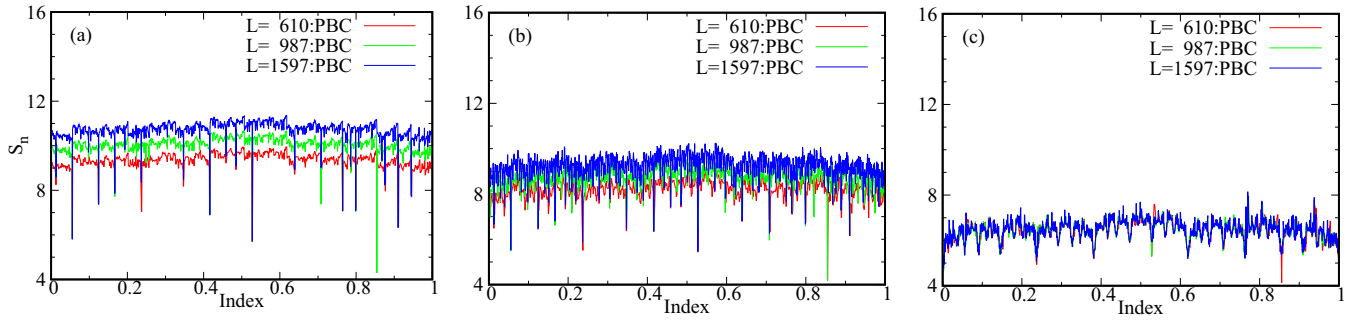

FIG. 8. Evolution of the von Neumann entropy S_n with an increasing disorder strength for a fixed RSO coupling $\alpha_z/t = 0.8$ and $\alpha_y = 0$. (a) $W/t = 2.5$, (b) $W/t = 2.55$, and (c) $W/t = 2.6$.

In Figs. 8(a)–8(c), the results of the von Neumann entropy calculations are presented for $\alpha_z/t = 0.8$ and $\alpha_y/t = 0.0$. To show the dramatic change in vNE as we move slightly away from the critical point ($W_c/t \simeq 2.55$), in Figs. 8(a) and 8(c), we have plotted our results for $W/t = 2.5$ and 2.6, respectively. It is clear that for $W/t = 2.5$, the von Neumann entropy increases with the system size and roughly scales as expected, while it is independent of the system sizes, and the value is close to zero for $W/t = 2.6$. It is clear from the results of Fig. 8(b) that at the critical point, these results do not completely follow the expected pattern of purely extended or localized states. These results, along with the localization tensor calculations and PR data, qualitatively capture the nature of the eigenstates at the critical point. However, it is necessary to have a more rigorous analysis to quantify the degree of multifractality of the eigenstates at the critical point. To address this, in the next section we have presented a detailed and careful analysis of the multifractal spectrum around the critical point.

VII. MULTIFRACTAL SPECTRUM AND THE QUASIPARTICLE EIGENSTATES

The "absence of length scale" at the critical point of a phase transition has led to the understanding that the concept of multifractals can be extended to analyze the critical properties [48,49]. This approach is quite general and has been used to study a wide range of problems in condensed-matter systems, such as the Anderson transition in different lattices [50,51], the localization-delocalization transition in quantum Hall systems [52], magnetization time series of the two-dimensional Ising model [53], conductance fluctuation in graphene [54], and transport properties in quasiperiodic systems [55], to name a few.

In multifractal analysis, the primary objective is to identify a local order parameter that could characterize the critical properties of a given system. The distribution of this local order parameter typically shows a fractal nature at the critical point. In the case of Anderson transition, the squared amplitude of the wave function plays the role of this local order parameter, and the distribution of the critical wave function has been found to be multifractal. Interestingly, the Anderson transition has been found in two dimensions in the presence of strong spin-orbit coupling, and in this case as well, the critical wave function has a multifractal character. In the case of the AAH Hamiltonian, all the wave functions at the critical point are multifractal in nature. From our localization-tensor calculations, we have found an identical signature of the metal-to-insulator transition in the AAH Hamiltonian in the presence of RSO coupling. Naturally, the question arises whether the critical wave functions also have multifractal character or not.

In contrast to a simple fractal structure, which is characterized by a single fractal dimension, a multifractal requires infinitely many exponents to characterize the complex distribution of the local order parameter. In our case, this can be achieved by identifying that $P(q)$, the qth moment of the probability of finding a quasiparticle within a linear box of length L ($L = Na$, $a = 1$ in arb. units), satisfies the following relation:

$$P(q) = \sum_{i=1}^{N} |\psi_n(i)|^{2q} \propto N^{-\tau(q)}, \tag{20}$$

where ψ_n is the quasiparticle wave function corresponding to the nth eigenvalue, and $\tau(q)$ is the q-dependent exponent that encodes the information about the fractal character of the wave function. In the case of multifractals, the infinite set of independent exponents $\tau(q)$ follows a nonlinear scaling relation in contrast to a normal fractal. The exponent $\tau(q)$ is alternatively expressed in terms of $D(q)$ as

$$\tau(q) = D(q)(q-1), \tag{21}$$

where $D(q)$ is called the generalized dimension. In the case of ergodic extended (EE) eigenstates, $\tau(q) = q - 1$ [50]. This conclusion follows from the argument that the real-space average $P(q)/N$ converges to the ensemble average $\langle P_q \rangle/N = \langle |\psi_n(i)|^{2q} \rangle$ in the limit $N \to \infty$ [56]. Effectively, it means that for EE states $D(q) = 1$, whereas for a completely localized eigenstate $D(q) = 0$. For multifractal states, $\tau(q)$ deviates from these two limiting cases, leading to q dependence of the generalized dimension $D(q)$. Out of the possible set of generalized dimensions, $D(2)$ is frequently used to characterize different states. In practice, however, instead of computing $\tau(q)$ directly, an equivalent quantity $f(\alpha)$ is evaluated. $f(\alpha)$ and $\tau(q)$ are connected by the Legendre transformation,

$$f(\alpha(q)) = q\alpha(q) - \tau(q), \tag{22}$$

where $\alpha(q) = d\tau(q)/dq$. In general, $f(\alpha)$ is a smooth non-monotonic positive valued function having negative curvature and a global maximum, but no local minima or maxima. In

fact, $f_{\max} = f(\alpha(q=0)) = d$, where d is the Euclidean dimension of the system [49]. From the analysis of the function $f(\alpha)$, one can easily identify the nature of the eigenstates. For EE states, in the large system size limit $f(\alpha = 1) = 1$, while $f(\alpha \neq 1) = -\infty$. For nonergodic (NE) eigenstates $f(\alpha(q)) \to 0$ for $0 < \alpha_{\min} < \alpha(q) < \alpha_{\max}$, while $f_{\alpha(q=0)} = f_{\max}$ appears when $\alpha(q=0) > 1$. In contrast to EE and NE states, for insulating states $f(\alpha(q)) \to 0$ as $\alpha(q) \to 0$, while $\alpha(q=0)$, i.e., the position of the maxima of the $f(\alpha)$ spectrum shifts toward a larger value than 1 as the disorder strength is increased. It is quite evident that to identify the nature of the quasiparticle eigenstates, it is sufficient to have an estimation of $\alpha_{\min}$ ($f(\alpha_{\min}) \to 0$) and $\alpha(q=0)$ [$f_{\max} = f(\alpha(q=0)) = d$]. This allows us to use a well-established method [49,57] to compute the multifractal spectrum for our Hamiltonian. This spectrum is computed and compared for both PBC and OBC. Both of these boundary conditions lead to identical conclusions.

A. Calculation of the multifractal spectrum

Before discussing the results, we briefly summarize the key steps to compute the multifractal spectrum. Initially, the lattice is divided into small boxes of linear size $l < L$. The first step is to find the normalized box-probability given by

$$\mathcal{P}_k(l,q) = \frac{\mathcal{P}_k^q(l)}{\sum_{j=1}^{N_b} \mathcal{P}_j^q(l)}, \tag{23}$$

where $1 \leqslant k \leqslant N_b = L/l$ represents the kth box and $\mathcal{P}_k(l,q) = \sum_{i \in l_k} |\psi_n(i)|^{2q}$, $l_k = l\,\forall\ k$, is the probability of the nth eigenstate. Then $\alpha(q,L)$ and $f(\alpha(q,L))$ are obtained from the following relations:

$$\alpha(q,L) = \lim_{\delta \to 0} \frac{\sum_{k=1}^{N_b} \mathcal{P}_k(l,q) \ln(\mathcal{P}_k(l,1))}{\ln \delta} \tag{24}$$

$$f(\alpha(q,L)) = \lim_{\delta \to 0} \frac{\sum_{k=1}^{N_b} \mathcal{P}_k(l,q) \ln(\mathcal{P}_k(l,q))}{\ln \delta}, \tag{25}$$

where $\delta = l/L$. It is important to note that this method of computing the multifractal spectrum is valid for $a \ll l < L$. For different system sizes L, we have chosen l in such a way that the above condition is satisfied and $0.1 \leqslant \delta \leqslant 0.5$. $\alpha(q,L)$ and $f(\alpha(q,L))$ have been computed for system sizes up to $L = 8 \times 10^3$, and averaged over the entire energy window up to the half-filling. Finally, the value of $\alpha(q) = \lim_{L\to\infty} \alpha(q,L)$ and $f(\alpha(q)) = \lim_{L\to\infty} f(\alpha(q,L))$ for a large system have been estimated using finite-size scaling [50]. It is important to note that, although we have not observed any kind of change in the qualitative nature in our large L limit results based on the system sizes used in our calculations, care should be taken while using the finite-size scaling to obtain the large-L limit result in the quasiperiodic systems [58,59]. For finite-size scaling, we propose the following set of functions for $\alpha_q(L)$ and $f(\alpha_q(L))$:

$$\begin{aligned} \alpha_q(L) &= \alpha_q + a_q L^{-1} + b_q L^{-2}, \\ f(\alpha_q(L)) &= f(\alpha_q) + c_q L^{-1} + e_q L^{-2}, \end{aligned} \tag{26}$$

where α_q, $f(\alpha_q)$, a_q, b_q, c_q, and e_q are all adjustable parameters. In Fig. 10, we present the scaled results of $\alpha_q(L)$ and $f(\alpha_q(L))$ for three different regions, i.e., at, above, and below the critical point. Before discussing the scaling results, we first discuss the $f(\alpha(q))$ versus $\alpha(q)$ spectrum, presented in Fig. 9. In Figs. 9(a)–9(c), we present the results for PBC, while the

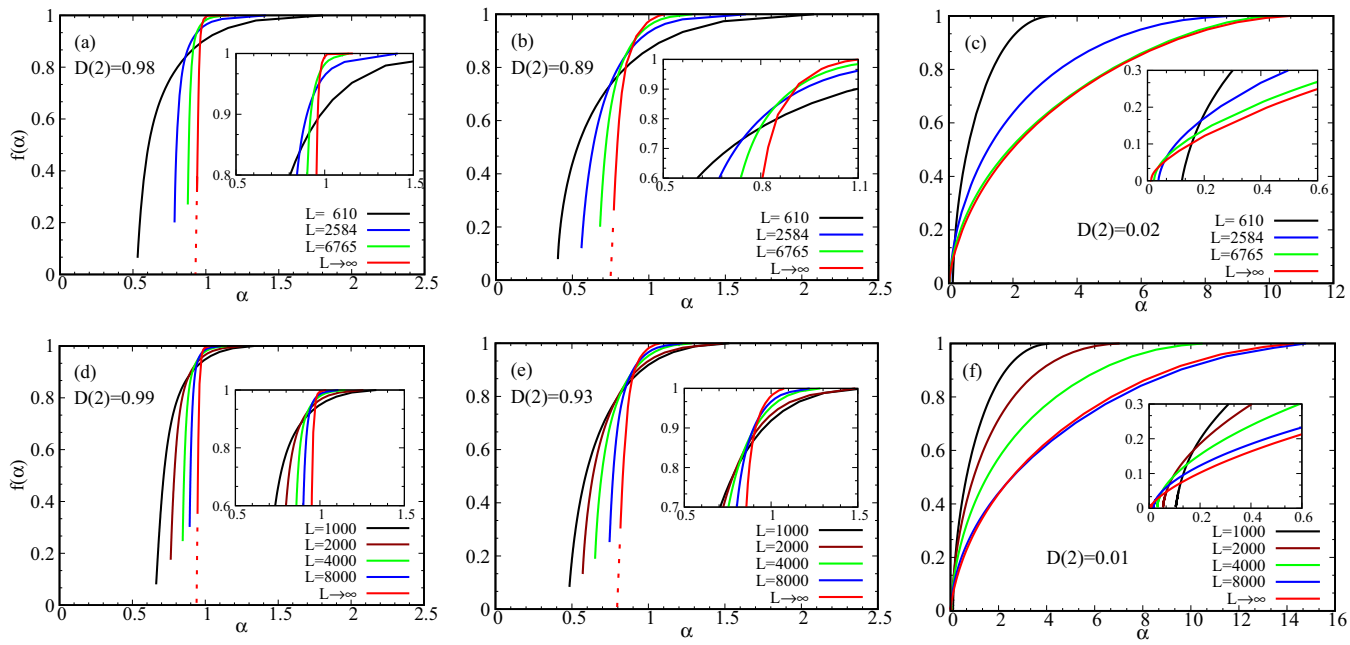

FIG. 9. Multifractal spectrum of the AAH Hamiltonian with RSO coupling for PBC (top row) and OBC (bottom row). Here, $\alpha_y/t = 0$ and $\alpha_z/t = 0.8$. From left to right: (a), (d) $W/t = 2.5$, (b), (e) $W/t = 2.55$, and (c), (f) $W/t = 2.6$. $D(2)$ is the generalized dimension $D(q)$ for $q = 2$. For extended ergodic states $D(2) = 1$, and $D(2) = 0$ for insulating states, while for multifractal/nonergodic extended states $0 < D(2) < 1$. The dotted lines in (a), (b), (d), and (e) are the linear extrapolation of the data (solid red line).

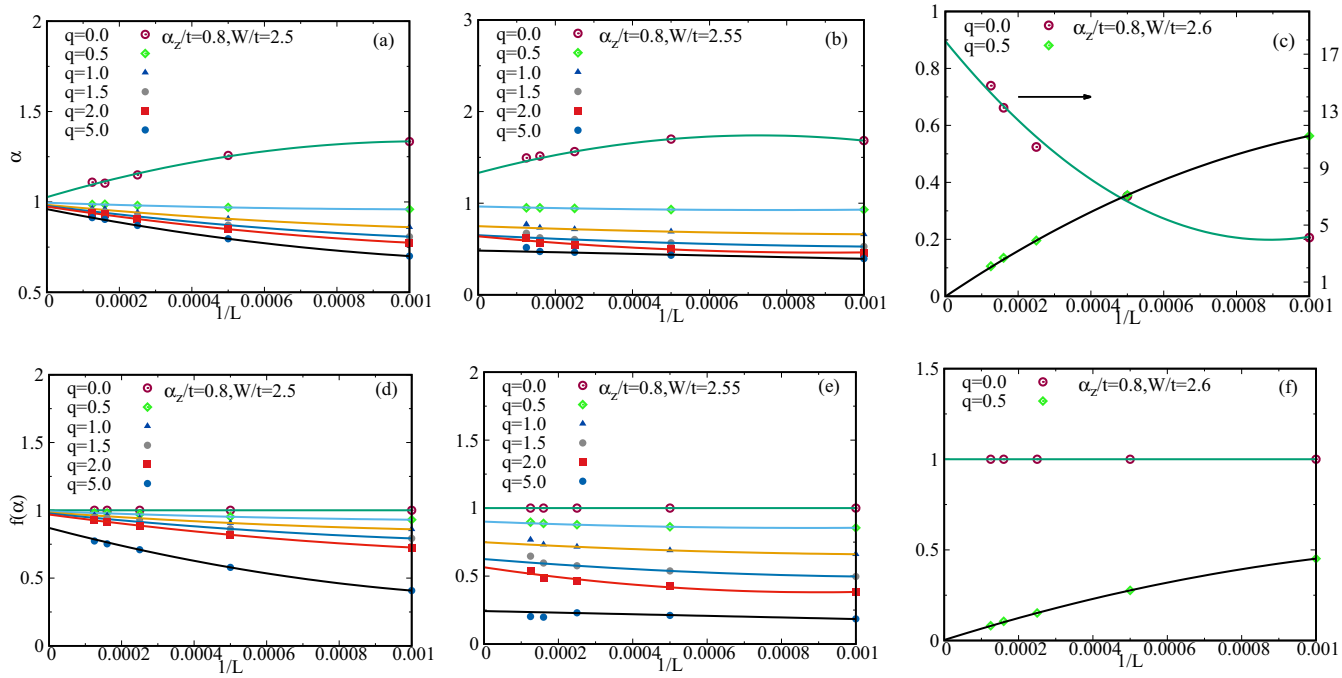

FIG. 10. Top row: the finite-size scaling of $\alpha(q)$ with $1/L$; and bottom row: the finite-size scaling of $f(\alpha(q))$ with $1/L$, for some limiting values of the moment q. The scaling functions are given in Eq. (26). The complex hopping amplitude $\alpha_y/t = 0$. From left to right, $W/t = 2.5$, 2.55, and 2.6. All of these results are presented for the open boundary condition.

results with OBC are presented in Figs. 9(d)–9(f). All these results are for $\alpha_z/t = 0.8$.

In Figs. 9(a) and 9(d), $\alpha_z/t = 0.8$ and $W/t = 2.5$. From the results of the localization tensor, the quasiparticle states are expected to be extended and ergodic. It is clear from the results of the multifractal spectrum that in the case of a large system size we have $f(\alpha(q = 0)) \to 1$, while $\alpha(q) \to 1$. These two values are not exactly 1, as one would expect for the case of ideal extended ergodic states, but they are very close to the ideal value. We have computed $D(2)$ using Eqs. (21) and (22). As expected for metallic states, our estimated value of $D(2)$ is 0.98 (0.99) for periodic (open) boundary conditions, respectively. As we increase W/t to 2.55 [Figs. 9(b) and 9(e)], we observe the dramatic change in the multifractal spectrum. When $L \to \infty$, $f(\alpha_q) \to 0$ for $\alpha(q) < 1$, while $f_{\max} = f(\alpha(q = 0)) = 1$ for $\alpha(q = 0) > 1$. This clearly indicates that all the states have multifractal character. This observation is also in close agreement with our estimated results of $D(2)$. At the critical point $D(2) = 0.89$ for PBC, while $D(2) = 0.93$ for OBC according to our estimate.

It is interesting to have a closer look at the behavior of $f(\alpha_q(L))$ versus $\alpha_q(L)$ spectra with a system size L. For different system sizes, the spectra cross each other at some point. How a spectrum moves with increasing system size on either side of the crossing indicates the nature of the eigenstates. For EE and NE states, the spectrum moves toward $\alpha = 1$ with increasing system size. This evolution of the multifractal spectrum with system size gets *reversed* quite dramatically as we increase the disorder strength just a little to the value $W/t = 2.6$. In this case, with increasing the system size, the spectrum moves toward $\alpha = 0$ on the left of the crossing point, while on the right of the crossing point it moves further away from $\alpha = 1$. The results are presented in Figs. 9(c) and 9(f). It is evident that as the system size increases, $f(\alpha_q) \to 0$ for $\alpha_q \simeq 0.0$, while $f_{\max} = f(\alpha(q = 0)) = 1$ for $\alpha(q = 0) \gg 1$, indicating that all the states are localized. From the numerical data, we find that $D(2) = 0.02$ (0.01) for PBC (OBC), as expected. These results are also consistent with our estimation of the critical point from the localization tensor calculations, as well as with the PR and vNE results.

In Fig. 10, we have presented the scaling data for $\alpha_y/t = 0$, $\alpha_z/t = 0.8$, and a few limiting values of q. Here, the results are presented for only OBC. For PBC, the results are nearly identical. To demonstrate the dramatic change in the multifractal spectrum, we have chosen the self-dual point $W_c/t = 2.55$, and two different potential strengths just below and above it. In Figs. 10(a)–10(c), $\alpha_q(L)$ has been plotted with $1/L$, while Figs. 10(d)–10(f) are for $f(\alpha_q(L))$. From Fig. 10(a), it is clear that just below the critical point $\alpha_q(L) \to 1$ with an increase in the system size for all q. The same pattern can be observed for $f(\alpha_q(L))$ as well, although for higher q the convergence is not perfect. The convergence of $f(\alpha_q(L))$ to 1 becomes perfect as the disorder strength is lowered slightly from $W/t = 2.5$. From Fig. 10(b), we can see that at the critical point, $\alpha_q(L)$ and $f(\alpha_q(L))$ do not converge to a single value for different q with the increase in system size. $\alpha_{q=0}(L)$ converges to a value greater than 1, while it converges to a single value much less than 1 as q increases beyond 2.0. At the same time, $\lim_{L\to\infty} f(\alpha_q(L)) \to 0$ as q is increased. This indicates that the eigenstates are extended but nonergodic. Quite dramatically, as W/t is increased just by a small amount to 2.6, $\lim_{L\to\infty}\alpha_{q=0}(L)$ converges to a value much larger than 1, while $\lim_{L\to\infty}\alpha_{q\neq 0}(L)$ and $\lim_{L\to\infty} f(\alpha_q(L))$ converge rapidly to the origin at the same time with higher

moment q. This indicates that the states are localized across the entire spectrum.

VIII. CONCLUSIONS

In conclusion, we have studied the effect of RSO coupling on the critical behavior of a one-dimensional quasiperiodic lattice, described by the AAH Hamiltonian. We have shown analytically that the RSO coupling terms do not break the self-dual nature of the AAH Hamiltonian. The critical points have been determined numerically with a high degree of accuracy with the help of the localization tensor. The results of the localization tensor, PR, von Neumann entropy, and multifractal analysis prove that the critical behavior is identical to the original AAH Hamiltonian. However, the self-dual and the critical points are not the same when all three hopping processes have nonzero amplitude. However, for the two limiting cases, when either the spin-conserving hopping or the spin-flip hopping processes are set to zero, the self-dual point and the critical point coincide with each other. Interestingly, when only the RSO Hamiltonian is considered with the quasiperiodic potential, the self-dual and the critical points get separated from each other. This indicates that the difference between the critical and self-dual point in the case of the full Hamiltonian is due to the combined effect of the two hopping processes of the RSO Hamiltonian. Generally, the critical point is pushed toward a higher strength of the quasiperiodic potential with an increase of the SO coupling strength. Furthermore, the above conclusions are independent of the filling fraction, unless the system is filled up to the special subgap states, which are actually localized at the boundaries, that might exist in the energy spectrum depending on the lattice size and the boundary conditions.

ACKNOWLEDGMENTS

This work is supported by the Science and Engineering Research Board (SERB), Department of Science and Technology, Government of India (Grant No. EMR/2015/001227).

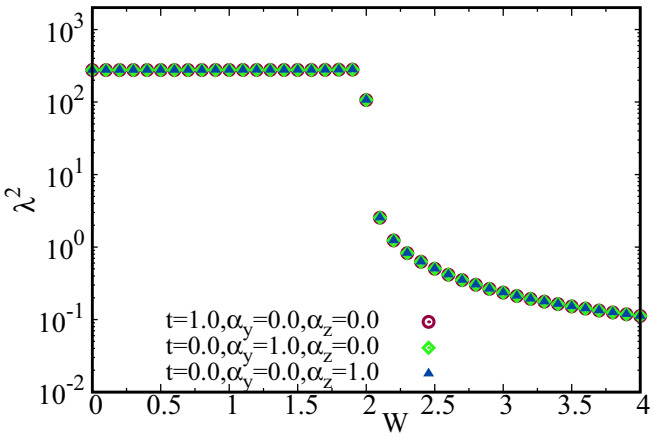

FIG. 11. The localization tensor results of a half-filled lattice for three cases: (i) $\alpha_y = \alpha_z = 0$, (ii) $t = 0, \alpha_z = 0$, and (iii) $t = 0, \alpha_y = 0$. To compute λ^2, we have used OBC and $L = 1597$.

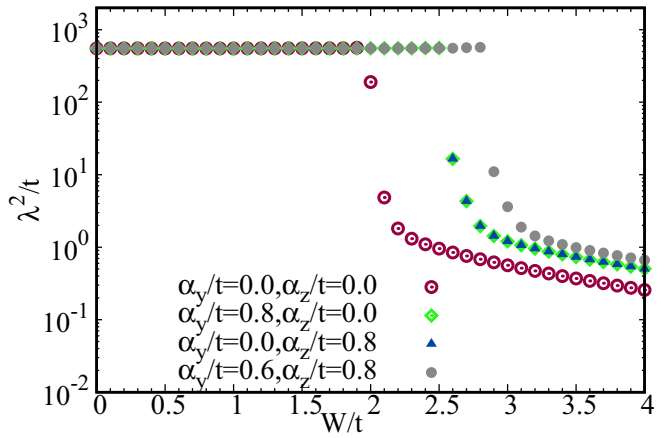

FIG. 12. The effect of RSO on the critical point is exactly the same at the quarter-filling. For $\alpha_y/t = 0$, $\alpha_z/t = 0.8$ and $\alpha_y/t = 0.8$, $\alpha_z/t = 0.0$, the critical point appears at the same point as in the half-filled case. This is true as well when both α_y/t and α_z/t are nonzero. Here, $L = 1597$.

S.D. would like to thank Aditi Chakrabarty for helpful feedback on the manuscript.

APPENDIX A

In Sec. III, we have stated that when each of the hopping processes is considered separately with the quasiperiodic potential, there is a self-duality exactly at $W/t = W/\alpha_y = W/\alpha_z = 2$. The metal-to-insulator transition is expected at the same disorder strength. In Fig. 11, we have verified this assertion numerically.

APPENDIX B

Our results are independent of the filling fraction. Here, we show the exact same trend in the critical point at quarter-filling. In Fig. 12, we have presented some representative results of our localization tensor calculations for $L = 1597$.

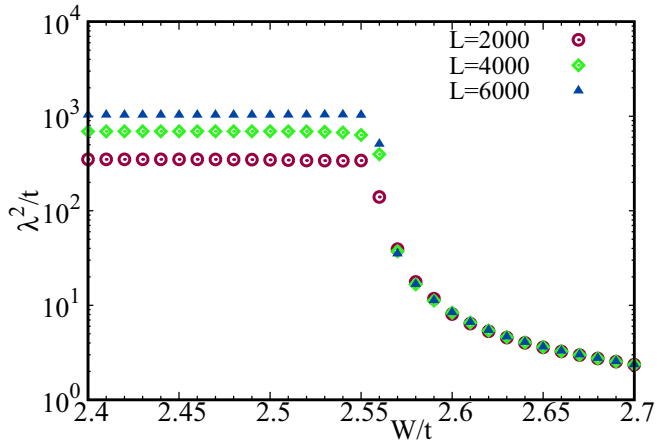

FIG. 13. It is clear that the transition happens between $W/t = 2.55$ and 2.57. The maximum error in determining the critical point is $\delta W_c/t = \pm 0.01$. OBC has been used to compute λ^2.

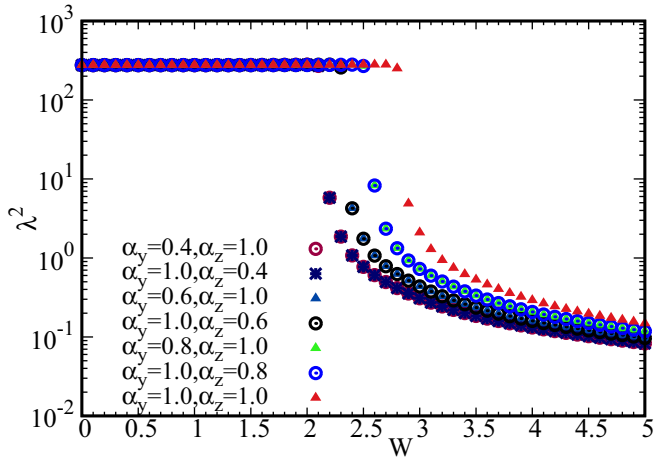

FIG. 14. The evolution of the critical point when t is set to zero. All the parameters of the Hamiltonian are measured in units of the parameter which is set to unity. We have used $L = 1597$.

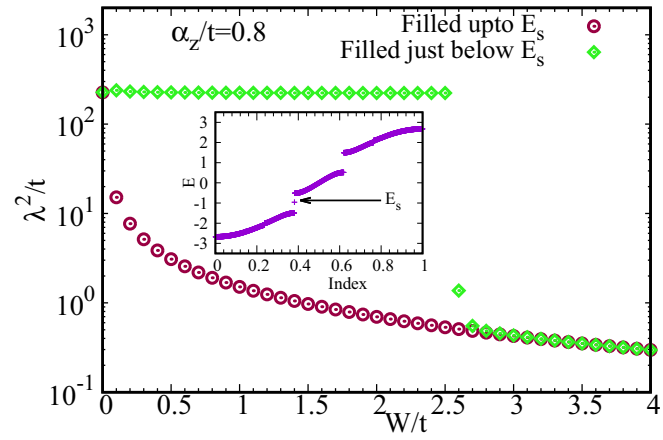

FIG. 15. The localization tensor for a lattice $L = 1000$ with OBC. The filling fraction has been fixed at the position where special state, E_s appear in the subband gap of the metallic states. The filling fraction up to E_S is 0.382. Here, $\alpha_y = 0$.

APPENDIX C

To demonstrate the accuracy of the numerical value of the critical point, in Fig. 13 we present the localization tensor results for increasing system sizes and $\Delta W/t = 0.01$. Similar calculations have been performed to determine the critical points presented in Table I.

APPENDIX D

From the discussion of the phase diagram, we have seen that the critical behavior is identical when only a pair of the hopping process is considered while the remaining hopping amplitude has been set to zero. In Sec. IV B, the results for two such cases have been presented. Here, we present the results for the third such case, that is, when the tight-binding hopping amplitude is set to zero. From Fig. 14, it is clear that the metal-to-insulator transition takes place at the same critical strength of the quasiperiodic disorder as that in Figs. 6(a) and 6(b).

APPENDIX E

In the quasiperiodic lattice, some electronic states may appear in the energy spectrum inside the subband gaps in the metallic phase. The appearance of these states is very sensitive to many factors, such as the lattice size, the boundary conditions, the quasiperiodic modulation controlled by the parameter b, etc. In Sec. V, we mentioned that these states do not affect the critical properties as long as the system is not filled up to this energy level. However, when the system is filled up to such special states, there is no metal-to-insulator transition. The localization tensor behaves identically to a 1D Anderson insulator [38]. In Fig. 15, we have plotted the localization tensor of a lattice of size 1000 when the system is filled up to the special state E_s, and just below E_s. λ^2 have been computed for $\alpha_y/t = 0$ and $\alpha_z/t = 0.8$. It can be clearly seen that the critical point is unaffected when the system is filled up to the state just below E_s. When the filling goes up to E_s, there is no metal-to-insulator transition.

[1] P. W. Anderson, Phys. Rev. **109**, 1492 (1958).
[2] E. Abrahams, P. W. Anderson, D. C. Licciardello, and T. V. Ramakrishnan, Phys. Rev. Lett. **42**, 673 (1979).
[3] P. G. Harper, Proc. Phys. Soc. London Sect. A **68**, 874 (1955).
[4] M. Ya. Azbel, Sov. Phys. JETP **17**, 665 (1963); **19**, 634 (1964); Phys. Rev. Lett. **43**, 1954 (1979).
[5] S. Aubry and G. André, Ann. Isr. Phys. Soc. **3**, 133 (1980).
[6] S. Hikami, A. I. Larkin, and Y. Nagaoka, Progr. Theor. Phys. **63**, 707 (1981).
[7] S. N. Evangelou and T. Ziman, J. Phys. C **20**, L235 (1987).
[8] S. N. Evangelou, Phys. Rev. Lett. **75**, 2550 (1995).
[9] T. Ando, Phys. Rev. B **40**, 5325 (1989).
[10] R. Merkt, M. Janssen, and B. Huckestein, Phys. Rev. B **58**, 4394 (1998).
[11] K. Minakuchi, Phys. Rev. B **58**, 9627 (1998).
[12] K. Yakubo and M. Ono, Phys. Rev. B **58**, 9767 (1998).
[13] Y. Asada, K. Slevin, and T. Ohtsuki, Phys. Rev. Lett. **89**, 256601 (2002).
[14] Y. Su and X. R. Wang, Phys. Rev. B **98**, 224204 (2018).
[15] M. Albert and P. Leboeuf, Phys. Rev. A **81**, 013614 (2010).
[16] M. Kohmoto and D. Tobe, Phys. Rev. B **77**, 134204 (2008).
[17] S. Sosa y Silva and F. Rojas, J. Phys.: Condens. Matter **24**, 135502 (2012).
[18] L. Zhou, H. Pu, and W. Zhang, Phys. Rev. A **87**, 023625 (2013).
[19] R. K. Malla and M. E. Raikh, Phys. Rev. B **97**, 214209 (2018).
[20] E. I. Rashba, Fiz. Tverd. Tela (Leningrad) **2**, 1224 (1960) [Sov. Phys. Solid State **2**, 1109 (1960)].
[21] I. Zutic, J. Fabian, and S. Das Sarma, Rev. Mod. Phys. **76**, 323 (2004).
[22] G. Roati, C. D'Errico, L. Fallani, M. Fattori, C. Fort, M. Zaccanti, G. Modugno, M. Modugno, and M. Inguscio, Nature (London) **453**, 895 (2008).

[23] Y. Lahini, R. Pugatch, F. Pozzi, M. Sorel, R. Morandotti, N. Davidson, and Y. Silberberg, Phys. Rev. Lett. **103**, 013901 (2009).
[24] Y. E. Kraus, Y. Lahini, Z. Ringel, M. Verbin, and O. Zilberberg, Phys. Rev. Lett. **109**, 106402 (2012).
[25] K. A. Madsen, E. J. Bergholtz, and P. W. Brouwer, Phys. Rev. B **88**, 125118 (2013).
[26] V. Goblot, A. Štrkalj, N. Pernet *et al.*, Nat. Phys. **16**, 832 (2020).
[27] Y.-J. Lin, K. Jimenez-Garcia, and I. B. Spielman, Nature (London) **471**, 83 (2011).
[28] P. Wang, Z.-Q. Yu, Z. Fu, J. Miao, L. Huang, S. Chai, H. Zhai, and J. Zhang, Phys. Rev. Lett. **109**, 095301 (2012).
[29] L. W. Cheuk, A. T. Sommer, Z. Hadzibabic, T. Yefsah, W. S. Bakr, and M. W. Zwierlein, Phys. Rev. Lett. **109**, 095302 (2012).
[30] J. E. Birkholz and V. Meden, Phys. Rev. B **79**, 085420 (2009).
[31] T. Ando and H. Tamura, Phys. Rev. B **46**, 2332 (1992).
[32] F. Mireles and G. Kirczenow, Phys. Rev. B **64**, 024426 (2001).
[33] Y. Cao, X. Gao, X. J. Liu, and H. Hu, Phys. Rev. A **93**, 043621 (2016).
[34] W. Kohn, Phys. Rev. **133**, A171 (1963).
[35] R. Resta, Phys. Rev. Lett. **80**, 1800 (1998).
[36] R. Resta and S. Sorella, Phys. Rev. Lett. **82**, 370 (1999).
[37] I. Souza, T. Wilkens, and R. M. Martin, Phys. Rev. B **62**, 1666 (2000).
[38] V. Kerala Varma and S. Pilati, Phys. Rev. B **92**, 134207 (2015).
[39] R. Resta, J. Phys.: Condens. Matter **14**, R625 (2002).
[40] R. Resta, Eur. Phys. J. B **79**, 121 (2011).
[41] R. Resta, J. Chem. Phys. **124**, 104104 (2006).
[42] G. L. Bendazzoli, S. Evangelisti, A. Monari, and R. Resta, J. Chem. Phys. **133**, 064703 (2010).
[43] S. N. Evangelou and J.-L. Pichard, Phys. Rev. Lett. **84**, 1643 (2000).
[44] Y. Takada, K. Ino, and M. Yamanaka, Phys. Rev. E **70**, 066203 (2004).
[45] K. Machida and M. Fujita, Phys. Rev. B **34**, 7367 (1986).
[46] N. Roy and A. Sharma, Phys. Rev. B **100**, 195143 (2019).
[47] F. Evers and A. D. Mirlin, Phys. Rev. Lett. **84**, 3690 (2000).
[48] T. C. Halsey, M. H. Jensen, L. P. Kadanoff, I. Procaccia, and B. I. Shraiman, Phys. Rev. A **33**, 1141 (1986).
[49] M. Janssen, Int. J. Mod. Phys. B **8**, 943 (1994).
[50] A. De Luca, B. L. Altshuler, V. E. Kravtsov, and A. Scardicchio, Phys. Rev. Lett. **113**, 046806 (2014).
[51] T. Nakayama and K. Yakubo, *Fractal Concepts in Condensed Matter Physics* (Springer, Berlin, 2003).
[52] F. Evers, A. Mildenberger, and A. D. Mirlin, Phys. Status Solidi B **245**, 284 (2008).
[53] L. Zhao, W. Li, C. Yang, J. Han, Z. Su, and Y. Zou, PLoS ONE **12**, e0170467 (2017).
[54] K. R. Amin, S. S. Ray, N. Pal, R. Pandit, and A. Bid, Commun. Phys. **1**, 1 (2018).
[55] J. Sutradhar, S. Mukerjee, R. Pandit, and S. Banerjee, Phys. Rev. B **99**, 224204 (2019).
[56] X. Deng, S. Ray, S. Sinha, G. V. Shlyapnikov, and L. Santos, Phys. Rev. Lett. **123**, 025301 (2019).
[57] E. Cuevas, Phys. Rev. B **68**, 024206 (2003).
[58] C. F. Moukarzel and G. G. Naumis, Phys. Rev. Lett. **115**, 209801 (2015).
[59] O. Stenull and T. C. Lubensky, Phys. Rev. Lett. **115**, 209802 (2015).